PG
Petroleum Geoscience

Research article

https://doi.org/10.1144/petgeo2020-014 | Vol. 27 | 2021 | petgeo2020-014

Influence of host rock composition on permeability reduction in shallow fault zones – implications for fault seal analysis (Vienna Basin, Austria)

Theresa Schröckenfuchs[1]*, Volker Schuller[1], Andras Zamolyi[1], Elias Mekonnen[1] and Bernhard Grasemann[2]

[1] OMV Exploration & Production GmbH, Trabrennstrasse 6–8, 1020 Vienna, Austria
[2] Department of Geodynamics and Sedimentology, University of Vienna, Althanstrasse 14, 1090 Vienna, Austria
* Correspondence: Theresa.Schroeckenfuchs@omv.com

Abstract: In order to calibrate equations for fault seal capacities to a specific basin, faults were analysed using core material from several Neogene hydrocarbon fields in the Vienna Basin, Austria. All studied specimens are siliciclastic rocks that were sampled from a depth interval of <2000 m, and share a similar depth at time of faulting, diagenetic conditions and maximum burial depth. Laboratory results showed a permeability reduction in all fault rocks compared to the host rocks. Both the highest and the lowest fault seal capacities were observed in the same fault rock type with a low phyllosilicate and clay content, and classifying as cataclastic deformation bands. Investigating the strong permeability variations within these fault rocks, microscopic analyses revealed that the fault seal potential is strongly linked to the detrital dolomite content in the host rock. Grain-size reduction processes occur preferably in the dolomite grains, accompanied by cementation. Our study suggests that – in addition to using standard fault seal analysis algorithms – accounting for host rock composition and grain-size reduction therein might help to further constrain fault seal behaviour in shallow depths. Fault seal mechanisms need to be understood on field, formation and micro scales before drawing conclusions for a full basin calibration.

Thematic collection: This article is part of the Fault and top seals collection available at: https://www.lyellcollection.org/cc/fault-and-top-seals-2019

Received 30 January 2020; **revised** 3 July 2020; **accepted** 31 August 2020

Algorithms and workflows for predicting fault seal behaviour in siliciclastic formations are well established and commonly used in standard software products for the petroleum industry (Allan 1989; Bouvier *et al.* 1989; Knipe 1992, 1997; Lindsay *et al.* 1993; Fristad *et al.* 1997; Yielding *et al.* 1997, 2010; Fisher and Knipe 1998; Manzocchi *et al.* 1999; Sperrevik *et al.* 2002; Yielding 2002; Bretan *et al.* 2003; Vrolijk *et al.* 2016; Bretan 2017; Ogilvie *et al.* 2020). Conducting fault seal analysis studies for the petroleum industry includes the calculation of fault rock attributes, which are calibrated using deterministic (Sperrevik *et al.* 2002) and empirical (Yielding 2002; Bretan *et al.* 2003) equations based on observations and measurements from known field data and field analogues around the world. The outcomes give a range of likelihood for fault seal capacity; however, this is accompanied with a broad range of uncertainty, since they are not calibrated to the respective area of interest.

To narrow the uncertainty range for fault seal capacity, a fault-seal calibration workflow can be conducted where software results are calibrated with core or field samples from the respective basin of interest. However, software results should not only be calibrated, but also critically reviewed with regard to the underlying algorithms and equations that were used to compute the software-based fault seal analysis.

The most commonly used standard software equations computing fault seal attributes for siliciclastic rocks are based on the concept of shale gouge ratio (SGR) (Fristad *et al.* 1997; Yielding *et al.* 1997; Freeman *et al.* 1998), an algorithm which mainly considers the mechanical mixing of host rock clay and phyllosilicate content into the fault rock (Fig. 1). At each point on the fault, the net content of phyllosilicates or clay in the volume of rock that has slipped past that point is calculated (Yielding 2002). The SGR algorithm assumes that material is incorporated into the fault rock in the same proportions as it occurs in the host rocks of the slipped interval. The key compositional component for the sealing potential is the clay or phyllosilicate content: small grain sizes lead to small pore throats and therefore to high capillary threshold pressure (Yielding *et al.* 2010). Yielding (2002) presented a compilation of fault data from fields in the Brent Province, Northern North Sea, suggesting that SGR values of *c.* 15–20% provide a threshold between sealing and leaking fault behaviour (0–20%, less likely to seal; 20–100%, more likely to seal). This threshold is commonly used in the petroleum industry for worldwide fault seal projects in basins with mixed clastic reservoirs. Furthermore, Fisher and Knipe (1998) suggested that SGR can also be interpreted as predicting fault rock types (Fig. 2). In simple fault zones, SGR (phyllosilicate) values of *c.* 15–20% are suggested to correspond to cataclasites or disaggregation zones, *c.* 20–40% to phyllosilicate framework rocks and SGR values of >40% are usually dominated by clay/shale smears (Fisher and Knipe 1998).

While increasing clay and phyllosilicate content shows a clear trend to decreasing fault permeability (e.g. Manzocchi *et al.* 1999; Crawford *et al.* 2002; Sperrevik *et al.* 2002; Childs *et al.* 2007; Yielding *et al.* 2010), several authors have pointed out the importance of diagenetic, compositional and textural effects on fault seal properties (e.g. Eichhubl *et al.* 2005; Exner *et al.* 2013; Griffiths *et al.* 2016; Vrolijk *et al.* 2016; Beke *et al.* 2019; van Ojik *et al.* 2019). These effects are not captured by SGR and are only partially considered in the existing algorithms that link SGR to the sealing capacity of faults.

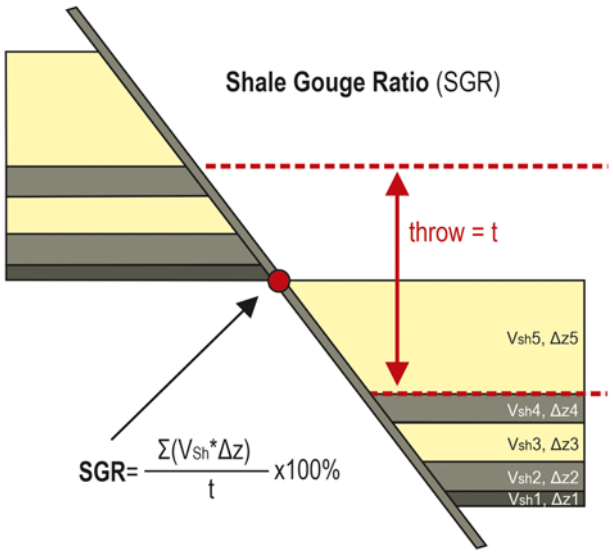

Fig. 1. Shale gouge ratio (SGR), after Yielding *et al.* (1997) and Freeman *et al.* (1998). For any point on the fault surface, the SGR is equal to the net shale/clay content of the rocks that have slipped past that point. The algorithm assumes that lithotypes are incorporated into the fault zone in the same proportions as they occur in the wall rocks, making SGR an estimate of the fault zone composition. In the equation V_{Sh} stands for the V_{shale} content of each bed/zone and Δz for the thickness. V_{shale} may be computed using gamma-ray logs, density/neutron logs or from core calibration using XRD analyses.

A deterministic equation published by Sperrevik *et al.* (2002) relates laboratory-measured variations in fault permeability and capillary pressure not only to the amount of clay phyllosilicates in the faulted sequence, but also to the depth of burial at time of faulting and the maximum burial depth. This partly accounts for diagenetic effects; however, Sperrevik *et al.* (2002) conducted their study with clean middle Jurassic sandstones of the North Sea where pervasive quartz cementation begins at temperatures of about 90°C, which corresponds to burial depths of about 3000 m (geothermal gradient of 30°C km^{-1}). The algorithm can therefore be used for similar clean and compositionally mature sandstone formations, but is not fully applicable for faults in siliciclastic formations with a higher content of other detrital minerals such as carbonates and weathered feldspars, or lithic fragments such as volcanic rocks where diagenetic effects or cataclasis might already have had a higher impact on sealing capacities in shallower reservoir depth intervals.

Another algorithm published by Bretan *et al.* (2003) is also based on SGR, which is empirically calibrated with pressure data to define depth-dependent seal-failure envelopes relating SGR to fault zone capillary entry pressure. The seal-failure envelope provides a generalized method, fitted for an exploration context, to estimate the maximum height of a hydrocarbon column that can be supported by a fault considering three different burial depth ranges: <3.0, 3.0–3.5 and >3.5 km. Again, the algorithm is mainly calibrated for clean sandstone formations, does not account for adjustment for possible diagenetic effects and is mostly fitted for an exploration context.

Conducting fault seal analysis studies in a production context for the Vienna Basin, Austria – a Miocene pull-apart basin located in Central Europe between the Eastern Alps and the Western Carpathians (e.g. Royden 1985; Ratschbacher *et al.* 1991; Linzer *et al.* 2002; Decker *et al.* 2005; Hinsch *et al.* 2005) – raised the need to reduce the uncertainties of the SGR-based approach. In order to narrow SGR ranges and define specific sealing capacities for faults in the Vienna Basin, faults were analysed using core material from several producing, siliciclastic hydrocarbon fields of Neogene age. Furthermore, an investigation on the significance of diagenetic and mineralogical effects impacting fault seal capacities was conducted. The focus was set on shallow reservoir levels. All studied specimens were sampled from a depth interval between *c.* 1600 and 2000 m measured depth (MD) from near-vertical wells to guarantee a comparability with regard to the depth range at the time of faulting, diagenetic conditions and maximum burial depths.

This paper outlines a full basin-specific fault seal calibration workflow; however, it focuses only on the laboratory calibration, sample analyses and discussion.

Reservoir property measurements (porosity, permeability) and mineralogical–geochemical analyses by X-ray diffraction analysis (XRD) of the studied core material are presented and integrated with petrographical thin-section descriptions of fault and host rocks (polarized light microscopy). Scanning electron microscopy (SEM) using secondary electron imaging was used to investigate possible small-scale fault rock cementation not resolvable with polarized light microscopy.

For the Vienna Basin, this study suggests a significant impact of host rock composition, grain-size reduction and diagenetic effects on the analysed fault/deformation band sealing capacities.

Since these processes are only partly covered by the standard fault seal analysis algorithms for siliciclastic rocks, this study emphasizes

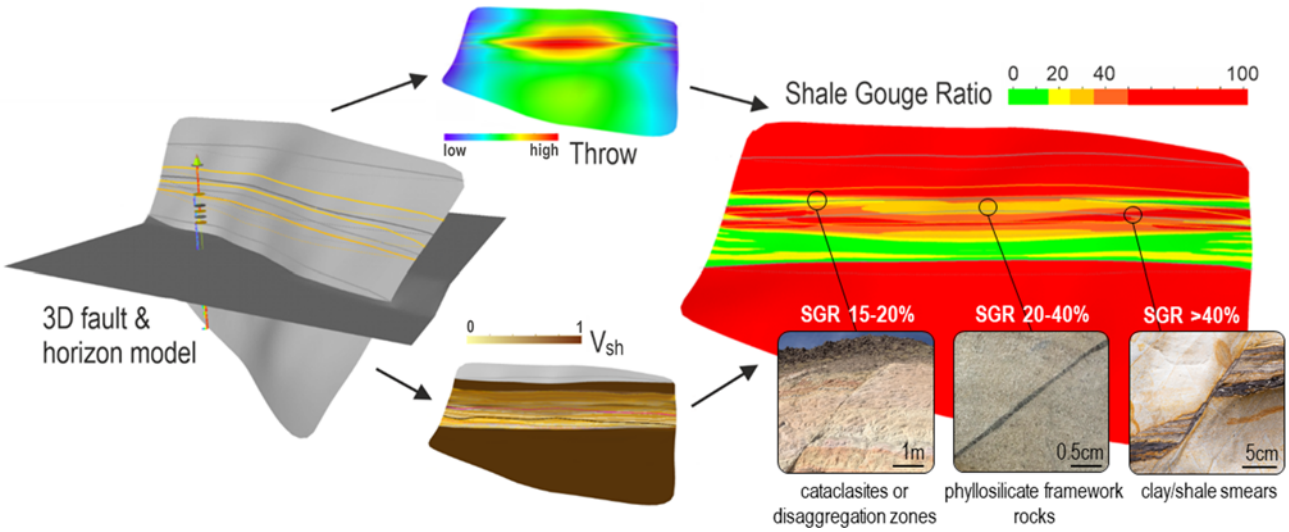

Fig. 2. Predicting fault rock types based on the SGR (Fisher and Knipe 1998). For simple fault zones, SGR values of 15–20% correspond typically to cataclasites or disaggregation zones, *c.* 20–40% to phyllosilicate framework rocks and values >40% to clay/shale smears (Fisher and Knipe 1998).

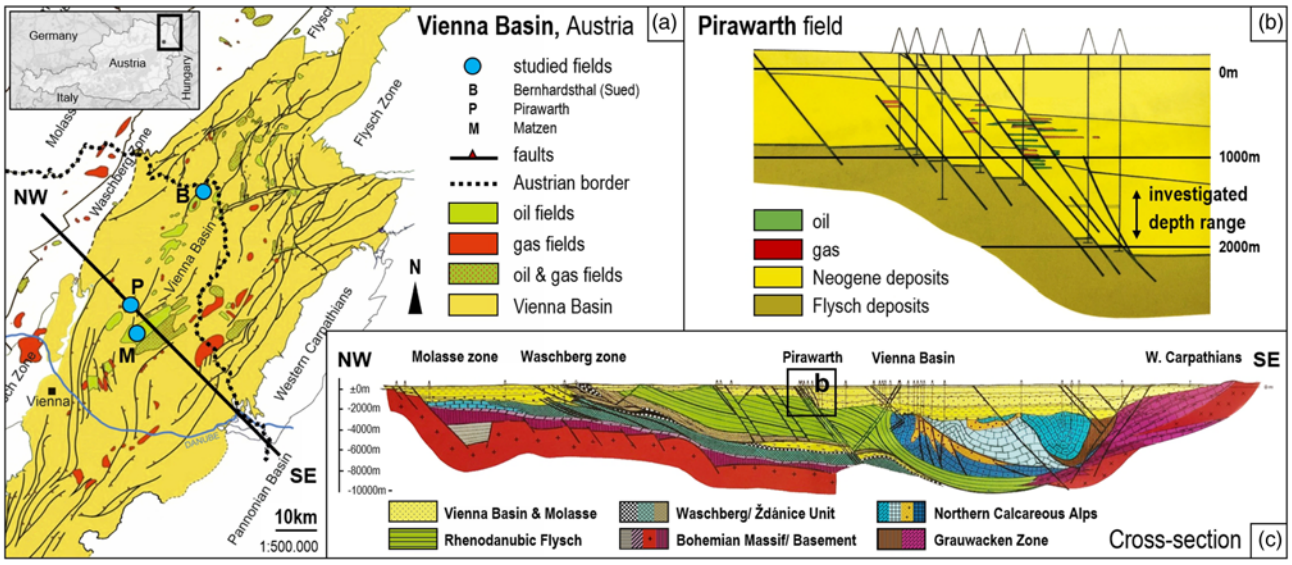

Fig. 3. (**a**) Overview of Austria and map of the Vienna Basin (modified after Arzmüller *et al.* 2006). Fields where cores were sampled are indicated with blue dots. (**b**) Cross-section of the Pirawarth Field, showing the NE–SW- and north-trending normal faults aligned in a stairstep pattern and the fault bounded reservoir character typical for the shallow Vienna Basin. The investigated depth area is 1600–2000 m and is constrained by available core data. (**c**) Cross-section through the Vienna Basin, indicating the location of the Pirawarth Field shown in (b); images (b) and (c) are modified after Wessely in Brix and Schultz (1993).

the importance of basin-specific fault seal capacity calibration. Furthermore, the presented laboratory measurements and the discussed processes aim to add publicly accessible data for a future development of the existing fault seal analyses and fault seal capacity algorithms. Algorithm adjustments for mineralogical composition and/or diagenetic processes are encouraged to allow more accurate fault seal predictions, especially for immature and lithic sandstones with low clay contents in shallow producing oilfields.

Basin-specific fault seal calibration workflow

Different levels of fault seal calibration can be applied to address the fault seal capacities in a specific basin: before calibration, fault seal analysis studies are conducted for several fields within the basin using the respective software packages and all available well log (V_{shale} log) and field data (oil density, pressure data). 3D fault models with Allan diagrams are computed – displaying fault attributes such as fault throw, bed juxtaposition and SGR.

The basic approach in the petroleum industry, which can be seen as a first level of calibration, uses the standard published empirical and deterministic equations proposed by Sperrevik *et al.* (2002), Yielding (2002) and Bretan *et al.* (2003). These equations are applied to calculate fault rock permeability and hydrocarbon column heights, and contain parameters that can be adjusted to the specific basin: the burial depth, the depth at time of faulting and the maximum burial depth during basin history. Under the condition that the tectonic basin history is understood and the lithology in the specific basin is relatively simple (clean sandstone–shale formations), results of this step are considered a calibration with basin-specific parameters based on global algorithms.

A more elaborate level of calibration can be conducted for basins where core data are available. It includes laboratory measurements on core plugs from the respective fields to measure permeability and clay content of the fault rocks. A statistically representative set of measured values can be used to set up a look-up function displaying the fault rock phyllosilicate (V_{shale}) content v. fault rock permeability. In theory, this correlation calibrates the software-calculated SGR values from the 3D fault models and incorporates basin-specific fault seal capacity variations caused by various mechanisms such as cataclasis or diagenesis (e.g. depth-dependent compaction or quartz cementation).

In the present study we show that for specific basins even the elaborate level of calibration might not be sufficient, since not all effects and fault rock mechanisms that influence fault seal capacity can be incorporated into a look-up function based on fault rock phyllosilicate content.

Therefore, in this paper our focus is solely set on the laboratory calibration, describing the core-plug sampling, methodology and analyses, followed by the presentation of results and a discussion of the basin-specific processes influencing fault seal capacity.

Focus area and geological setting of samples

The laboratory-based fault seal calibration was conducted for the Vienna Basin (Fig. 3), a rhomboedric, 200 km-long and 60 km-wide classic pull-apart basin between the Eastern Alps and the Western Carpathians, which formed along sinistral strike-slip fault systems during the Miocene lateral extrusion of the Eastern Alps (e.g. Royden 1985; Ratschbacher *et al.* 1991; Linzer *et al.* 2002; Decker *et al.* 2005; Hinsch *et al.* 2005). The tectonic history of the Vienna Basin can be divided into four major steps (e.g. Royden 1985; Jiřiček and Seifert 1990; Ratschbacher *et al.* 1991; Decker 1996; Peresson and Decker 1997; Decker *et al.* 2005): (1) formation of a piggyback basin (Lower Miocene); (2) formation of a pull-apart basin (Middle–Upper Miocene); (3) east–west compression and basin inversion (Upper Miocene); and (4) east–west extension (Pleistocene–Recent). Hydrocarbon migration from Upper Jurassic source rocks occurred predominantly syn- to post-tectonically in multiple stages along vertical pathways bound to synsedimentary structures and normal fault systems (Ladwein 1988; Francu *et al.* 1996; Arzmüller *et al.* 2006; Rupprecht *et al.* 2019). Focus was set on core material from Lower–Middle Miocene formations deposited during piggyback and pull-apart stages of the Vienna Basin (Strauss *et al.* 2006). All studied fields (Fig. 3a) are bound by conjugated normal fault systems (Fig. 3b) which are linked to Middle–Upper Miocene pull-apart and NW–SE extension phases, and are clearly visible on seismic (Hinsch *et al.* 2005). Cores from different fields were chosen to sample a broader variety for the fault seal calibration workflow: the

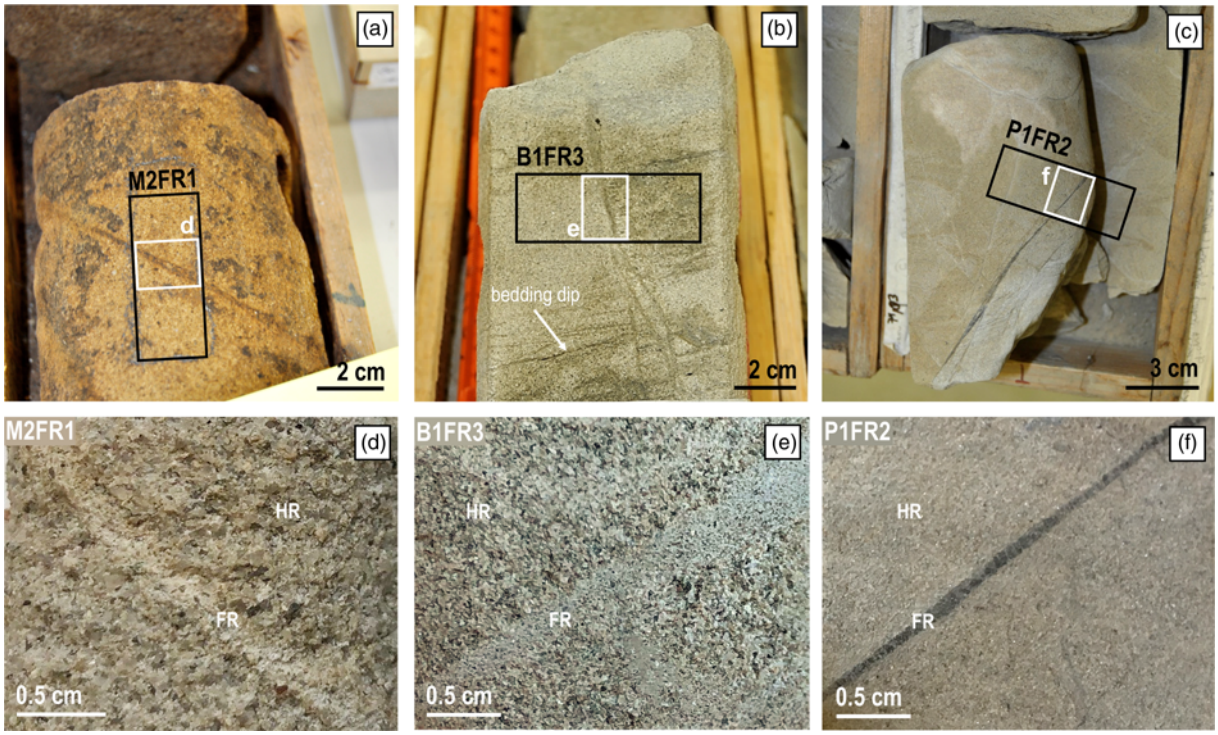

Fig. 4. Overview of selected core material and detailed view of the fault rock plugs. Samples M2FR1 (**a**) & (**d**) and B1FR3 (**b**) & (**e**) are classified as cataclastic deformation bands. Sample P1FR2 (**c**) & (**f**) is classified as a phyllosilicate band. Detailed views of the drilled plugs displaying both host rock and fault rock are shown in (d)–(f). Please note that the cores in (a) & (b) show oil impregnation (brownish stain), whereas the photographs in (d) & (e) were taken after sample cleaning. HR, host rock; FR, fault rock.

Bernhardsthal and Bernhardsthal Sued Field, the Pirawarth Field, and the Matzen Field (Fig. 3a). The latter is still regarded to be the aerially largest onshore oil and gas field of Central Europe, and produced more than 510 MMSTB of oil and 1.2 TCF of gas since 1949 (Schumi and Gager 2002). The Matzen Field can be divided into four different structural zones: (1) a NE–SW-trending anticline in the central part of the field; (2) the Matzen Fault Zone in the north of the field, a pull-apart graben system bounded by sinistral strike-slip faults; (3) the Bockfliess Fault System in the west; and (4) the Markgrafneusiedl normal fault zone in the south (Schroeckenfuchs 1975; Fuchs and Hamilton 2006; Exner *et al.* 2013). The studied samples in the Matzen area are related to the Bockfliess normal fault system.

The Pirawarth Field started production in 1964 (Poellitzer *et al.* 2009). It is located NW of the Matzen Field, and structurally consists of a set of NE–SW- and north-trending normal faults (Fig. 3b), aligned in a stairstep pattern and dipping towards the SE to east (Brix and Schultz 1993) – all linked to the larger Steinberg fault system, which reaches maximum offsets of 5.6 km (Lee and Wagreich 2017).

The Bernhardsthal Field was discovered in 1950, Bernhardsthal-Sued started production in 1986 (Brix and Schultz 1993). Both fields are located close to the Czech border in the NE corner of the Vienna Basin and are bounded by the Steinberg Fault System – roughly striking in a SSW–NNE direction (Harzhauser *et al.* 2018) at the field locations.

All sampled cores consist of siliciclastic sand, shale and marl formations from mainly marine depositional environments – mostly deltaic deposits (Sauer *et al.* 1992). The studied reservoir sandstones classify as (sub)lithic arenites (Pettijohn *et al.* 1973) with varying occurrences of detrital carbonate lithic fragments, which were presumably eroded from relatively proximal mountain belts such as the Northern Calcareous Alps (Gier *et al.* 2008). All studied wells are nearly vertical and bedding dips are near-horizontal in the studied cores (Fig. 4b).

Sampling was restricted to a depth range between *c.* 1600 and 2000 m MD to focus on shallow siliciclastic reservoirs (<2 km), and to guarantee the comparability of samples for fault seal analysis in terms of tectonic and diagenetic history, depth at time of faulting, and burial depth.

Laboratory methodology and analysis

All analysed samples are listed in Table 1. Initially, 32 samples from five wells were chosen from available core material (Fig. 4a–c). For each investigated depth a pair of core plugs (1 inch diameter) was selected, where one plug captures fault rock with its surrounding host rock (Fig. 4d–f), and the other plug consists solely of host rock. Plugs were drilled perpendicular to the fault/deformation band dip (Fig. 4a–c). Five fault rock samples were damaged during plugging (i.e. no representative cylindrical volume could be sampled due to breakage along the fault or dismembering of the host rock). Therefore five sample pairs could not be used for further analysis.

All samples were cleaned prior to investigation using Soxhlet extraction (Soxhlet 1879) to remove water and oil. The core-cleaning solvents were chloroform and methanol azeotrope with a boiling point of 54°C. After cleaning, the samples were dried in a vacuum at 60°C. The method ensures that the plug samples are cleaned, but heated to a minimum.

For the intact host rock plugs, effective porosity (PHIE) was determined by helium expansion (Table 1). Permeability was measured for the fault rock and host rock plugs (Table 1) using bottled nitrogen under steady-state conditions and applying a confining pressure of 3.5 MPa. To compute the fault rock permeability, measurements obtained from the plugs consisting solely of host rocks were subtracted from the plug measurements containing both host and fault rock. Subsequently the plugs were cut in half.

One half plug was manually prepared, powdering host rock and fault rock material separately for X-ray diffraction analysis (XRD) in order to determine the bulk mineralogical composition, as well as the

Table 1. *Measurement results of analysed samples, sorted by well name and depth*

						XRD results (wt%)									
Well name*	Sample name[‡]	Depth (m, MD)	PHIE (%)	*K* (mD)	*K* reduction factor	Quartz	K-felspar	Plagioclase	Calcite	Dolomite	Ankerite	Siderite	Pyrite	Clay total and mica	Classification[‡]
M1	M1FR1	1644.00	–	928.47	2	82.1	3.4	5.7	3.2	2.4	0.7	–	0.1	2.4	Cataclastic band
M1	M1HR1	1644.00	29.75	1616.68		83.2	3.4	5.1	3.2	1.3	0.8	0.1	0.1	2.8	
M2	M2FR1	1645.70	–	35.00	6	64.6	4.0	1.4	17.4	3.4	4.5	0.5	0.2	4.1	Cataclastic band
M2	M2HR1	1645.70	22.20	193.14		69.7	3.3	2.6	18.6	0.8	1.4	0.3	0.2	3.1	
M2	M2FR2	1654.40	–	639.00	3	82.7	4.3	0.7	7.3	1.3	1.2	–	–	2.5	Cataclastic band
M2	M2HR2	1654.40	27.71	2210.80		80.1	3.4	0.5	8.7	2.6	1.6	–	–	3.0	
M3	M3FR1	1706.80	–	19.79	5	86.5	3.3	0.6	3.1	3.1	1.6	–	–	1.8	Cataclastic band
M3	M3HR1	1706.80	26.09	95.32		84.2	3.1	1.2	2.5	4.2	3.0	–	0.1	1.7	
B1	B1FR1	1849.20	–	17.07	21	57.1	3.8	6.6	6.2	11.9	11.6	–	0.4	2.4	Cataclastic band
B1	B1HR1	1849.20	24.24	355.08		58.9	4.1	8.3	7.3	10.3	4.9	0.2	0.5	5.5	
B1	B1FR2	1850.20	–	0.60	143	60.3	1.6	5.0	6.7	10.7	10.3	1.0	0.6	3.8	Cataclastic band
B1	B1HR2	1850.20	18.61	85.77		63.5	2.3	4.4	6.5	11.4	6.1	0.5	0.3	5.0	
B1	B1FR3	1851.70	–	0.50	913	61.7	2.8	5.4	6.0	13.6	7.1	–	0.4	3.1	Cataclastic band
B1	B1HR3	1851.70	22.14	456.73		66.5	3.2	5.4	5.1	13.6	2.9	0.2	0.8	2.4	
B1	B1FR4	1854.20	–	2.30	48	49.1	1.4	2.6	4.4	13.6	6.2	1.2	1.0	20.5	Phyllosilicate band
B1	B1HR4	1854.20	18.18	109.45		46.3	2.1	6.2	8.1	18.9	5.8	0.6	0.4	11.6	
B1	B1FR5	1854.30	–	0.28	1168	62.5	1.9	3.3	9.7	11.1	7.7	0.2	0.4	3.2	Cataclastic band
B1	B1HR5	1854.30	24.16	326.90		63.6	1.6	5.3	7.2	11.2	2.4	0.3	0.8	7.7	
P1	P1FR1	1850.20	–	1.21	5	45.7	2.3	8.2	8.7	14.0	0.8	0.8	0.4	19.1	Phyllosilicate band
P1	P1HR1	1850.20	17.20	6.04		51.0	2.3	7.3	11.2	8.9	2.0	0.4	0.2	16.7	
P1	P1FR2	1971.10	–	0.97	5	54.4	1.8	5.7	5.8	12.6	–	1.3	0.2	18.2	Phyllosilicate band
P1	P1HR2	1971.10	21.01	5.33		56.7	2.3	8.4	9.5	9.2	0.9	1.5	0.2	11.4	

*Well names were adapted for publication due to confidentiality reasons and in order to match the field name abbreviations used in Figure 3.
[†]FR, fault rock; HR, host rock.
[‡]Classification after Fossen and Bale (2007).

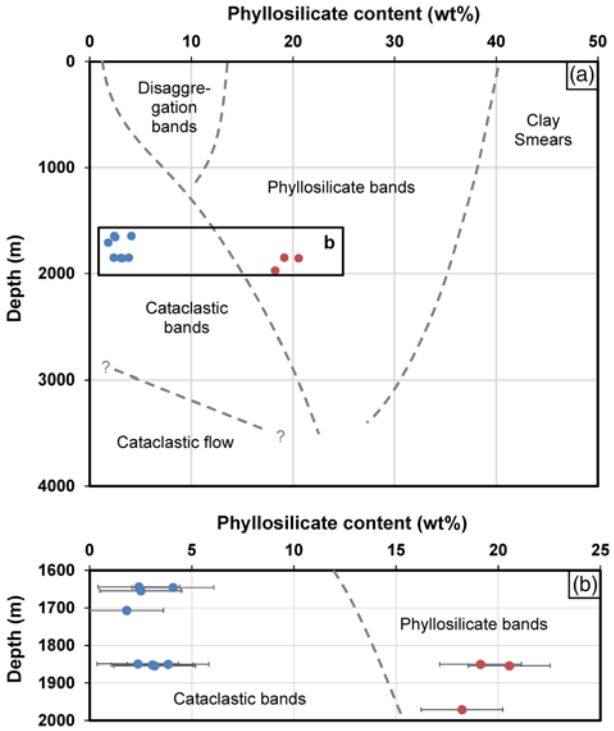

Fig. 5. (**a**) The studied samples are plotted on a graph modified after Fossen and Bale (2007) differentiating deformation band types by phyllosilicate content and depth. Two groups can be distinguished: cataclastic band samples with a low phyllosilicate content; and phyllosilicate band samples with a phyllosilicate content of *c*. 20%. (**b**) Detailed view of the sample range. Error bars indicate an absolute XRD analytical uncertainty of 2%.

clay total and mica content in the host and fault rock (Table 1). The XRD analyses were conducted using a Bruker AXS D8 Advance XRD spectrometer (copper radiation-generated X-ray tube at 40 kV and 40 mA, and X-ray detector Lynxeye XE-T). The Bruker software program DIFRAC.EVA V3 was used to identify the different mineral phases. The quantification of minerals detected by XRD is based on peak heights within the spectrum based on the method of Schultz (1964) and OMV internal standards. Based on comparison with other methods and other laboratories, the quantification results show an absolute measurement error range of *c*. 2% (Fig. 5b).

The other half of the plug was used for thin-section preparation. The thin sections were vacuum impregnated with blue epoxy resin to enable the study of pore space. Additionally, they were stained with a combination of Alzarin Red-S and potassium ferricyanide (Dickson 1965) for the identification of carbonate mineralogy. After staining, Fe^{2+}-free calcite appears pale pink to red, ferroan calcite purple to mauve-blue, Fe^{2+} dolomite shows no staining, and ferroan dolomite or ankerite displays pale to deep turquoise colours depending on the ferroan content.

Petrographical thin-section analysis was performed and documented with a Leica DM 2500 P polarized-light microscope equipped with a Jenoptik Gryphax microscope camera. The host rock modal composition was determined by counting 300 points per thin section. Additionally, petrographical sample analyses included a detailed analysis of deformation microstructures within the deformation bands.

Undestroyed remains from the XRD-measurement half plugs were broken into small rock chips with freshly broken surfaces including both fault and host rock. The samples were mounted with conductive glue onto aluminium pin stubs, and gold coated prior to analysis with a Zeiss 1450 EP and a Tescan Mira 3 scanning electron microscope using secondary electron imaging. SEM analysis was used to provide a 3D view of the pore space, and to investigate possible fault rock cementation and minerals not resolvable with the polarized light microscope.

Petrophysical sample properties and geochemistry results (XRD)

Porosity, permeability and geochemical measurement (XRD) results for all samples are listed in Table 1. When plotted for phyllosilicate content (clay total and mica content, XRD) v. depth (Fig. 5a), the analysed samples can be categorized into two groups after Fossen and Bale (2007): cataclastic deformation bands with very low clay and mica contents of between 1.8 and 4.1 wt%; and phyllosilicate bands with clay and mica contents ranging from around 18 to 20.5 wt%.

A permeability decrease from host rock to fault rock can be observed for all studied samples (Table 1; Fig. 6a). Data analysis shows that the greatest permeability reduction from host rock to fault rock is not observed in the phyllosilicate bands with elevated clay contents, but in the cataclastic band samples with low clay contents (Fig. 6b). While the studied phyllosilicate band samples show a permeability reduction factor of 5–48 (Table 1), the cataclastic band sample B1HR5–B1FR5 shows a reduction in permeability from 326.9 mD in the host rock to 0.28 mD in the fault rock, which corresponds to a permeability reduction factor of 1168. However, a large variation in permeability reduction can be observed within the cataclastic band samples (Fig. 6b), suggesting that there is a subgroup with a quite low permeability reduction factor (3–6) and another subgroup that displays a higher permeability reduction factor (21–1168). A thorough analysis of XRD results indicated elevated dolomite contents (10.3–13.6 wt%) in host and fault rocks of the samples with a high permeability reduction factor (Fig. 6c). Additionally, the ferroan dolomite or ankerite content rises from the host rock (2.4–6.1 wt%) to the fault rock (7.1–11.6 wt%). Conversely, the samples with a low permeability reduction factor have a dolomite content in the range of 0.8–4.2 wt%, and low ferroan dolomite or ankerite contents in the host and fault rocks (<4.5 wt%). In order to investigate the underlying mechanism for the observed variability in permeability and the strongly varying distribution of carbonates in the geochemistry results, all cataclastic band samples were further analysed in thin sections.

Petrographical thin-section description

Cataclastic band sample set with small permeability reduction

Modal analysis in the host rocks of the cataclastic band samples with a small permeability reduction show a detrital grain framework (Fig. 7a–c) that is composed of quartz and lithic fragments, which are mainly quartzite grains (82–87%), minor amounts of feldspar (3–5%), plagioclase (1–5%), carbonates (mainly calcite and dolomite: 5–10%) and clay/mica (2–3%). The samples classify as weakly cemented, medium-grained, moderately sorted sublithic arenites (Pettijohn *et al.* 1973). Calcite occurs as detrital grains and as cement bridging detrital grains within the host rock grain framework (Fig. 7c). Detrital dolomite occurs subordinately. In contrast to the other samples in this group, sample M2FR1–M2HR1 shows a greater amount of calcite cement (15%).

The fault rocks within the deformation bands consist of host rock grains that exhibit transgranular fracturing (Fig. 8a–d), where fractures split grains into more evenly sized smaller parts. Furthermore, flaking can be observed, where microfractures form close to the grain surface and result in the chipping off of parts of the grain (Fig. 8a–c). The majority of the newly formed grains exhibits angular grain shapes. Quartz grains show a clear reduction in grain

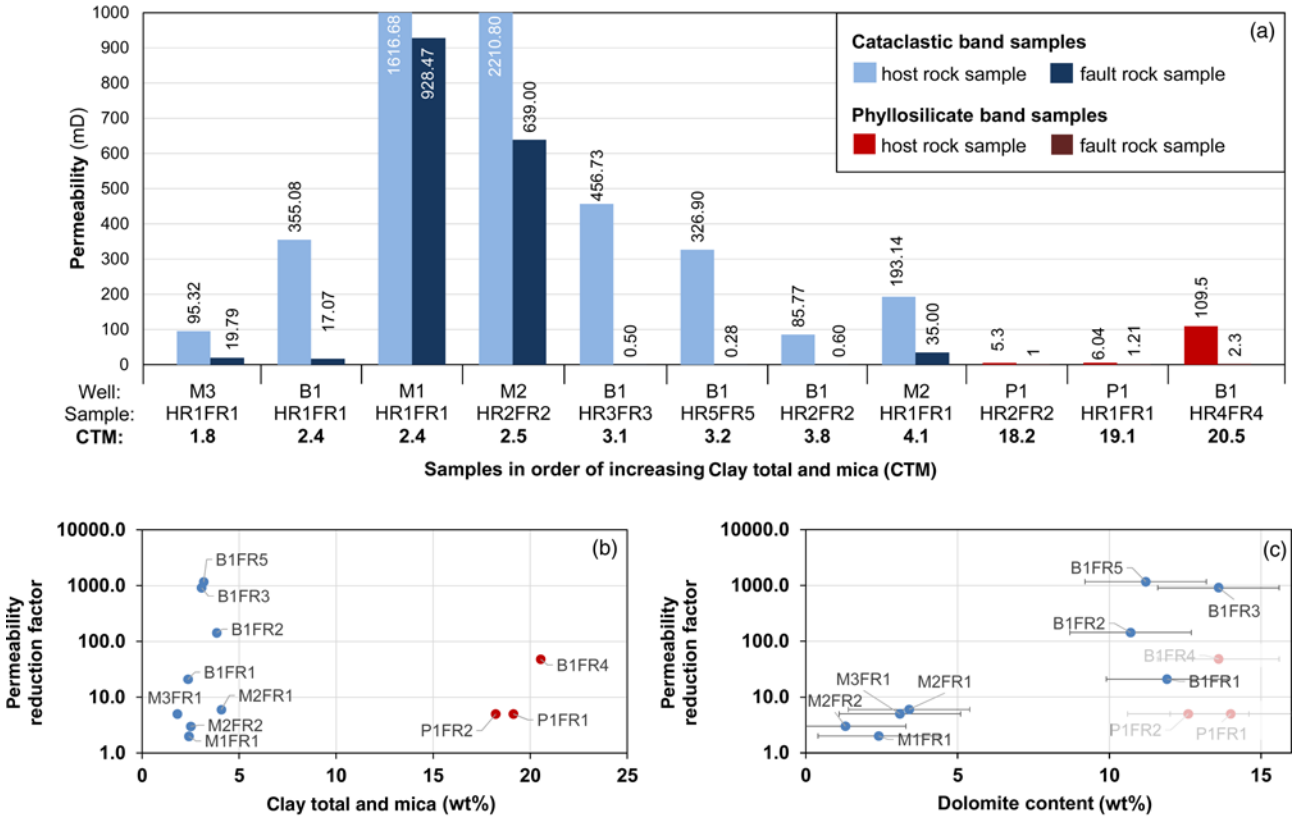

Fig. 6. (**a**) Plug-permeability measurements plotted against fault rock clay and mica content. XRD results are assumed to represent V_{shale}. Respective permeability values are plotted above or in the bars. A clear permeability reduction for all sample pairs is visible. The well name, sample name, and clay total and mica content are listed below the respective bars along the *x*-axis. HR, host rock; FR, fault rock. (**b**) Permeability reduction factor plotted against clay total and mica content (XRD). The highest and lowest permeability reduction occurs in the cataclastic band samples (blue). (**c**) Permeability reduction factor v. dolomite content from XRD. The phyllosilicate samples are plotted for completeness but are not discussed as they are dominated by another deformation process (platy minerals support grain sliding). Sample B1FR1 plots slightly outside the data trend; however, due to a discontinuity in the deformation band, the values are not seen as the maximum possible reduction factor.

size – decreasing down to 5–10 μm (Fig. 7d). Patchy, small-scale calcite cementation starts around crushed calcite grains; however, a large amount of remaining porosity is clearly visible in the fault rock (Fig. 7d). SEM analyses were conducted to detect possible additional small-scale cement that was not resolvable in polarized light microscopy. The analyses confirmed the thin-section observations and clearly showed open pore space within the fine-grained cataclastic matrix (Fig. 9b).

Cataclastic band sample set with a large permeability reduction

Modal analysis in the host rocks of the cataclastic band samples with a large permeability reduction (Fig. 7e–g) are composed of detrital quartz and lithic fragments (mainly quartzite grains: 55–70%), large amounts of carbonates (mainly dolomite, ferroan dolomite and calcite: 21–32%), feldspar (1–4%), plagioclase (3–8%) and clay/mica (2–4%). The host rock samples classify as weakly cemented, medium-grained, moderately- to well-sorted sublithic arenites (Pettijohn *et al.* 1973). As indicated by the XRD results, the carbonate content – especially dolomite – of the host rock is significantly elevated. The dolomite rock fragments in the host rock are dolosparite and dolomicrosparite (Fig. 7g). Detrital dolomite grains partially exhibit cement rims of ferroan dolomite (Fig. 8f). However, the cement rims reduce the host rock pore space insignificantly. Calcite occurs subordinately as bridging cement or detrital calcisparite.

Fault rocks in the deformation bands of the large permeability reduction sample set are composed of a fine-grained matrix, consisting of crushed (mainly dolomitic: Fig. 8g and h) grains, filling the pore space between components of partially undestroyed or minor crushed quartz grains from the host rock (Fig. 7h). Larger carbonate survivor grains are present (Fig. 8g and h); however, the amount of larger carbonate grains in the fault rock decreases by an order of 10 compared to the host rock. No porosity is visible in polarized light thin-section microscopy.

SEM analysis of the fine-grained fault rock matrix shows that dolomite and ferroan dolomite cementation is occurring in addition to grain crushing on a micro scale. The newly grown dolomite crystals do not exceed crystal sizes of a few micrometres (Fig. 9d–f) and close most of the remaining pore space between the fine-grained crushed matrix (Fig. 9d–f). The euhedral dolomite crystals show flat faces with sharp angles and rhomboedric crystal shapes (Fig. 9f) – both indications that they are not comminuted grains (Fig. 8e) but rather newly grown cement.

Discussion

Thin-section observations and XRD results show a correlation between host rock dolomite content and fault rock permeability in the studied samples (Fig. 6c). The low-permeability fault cores are clearly visible (Fig. 10) in UV light pictures of oil-stained core material taken before the sampling: while the host rock is clearly oil impregnated, no impregnation is visible within the fault rock/deformation band clusters.

A combination of processes leading to a large permeability reduction in the fault rock is suggested:

(1) mechanical grain-size reduction – supported by a hardness contrast between the quartz and carbonate grains (preferred cataclasis of weaker grains);

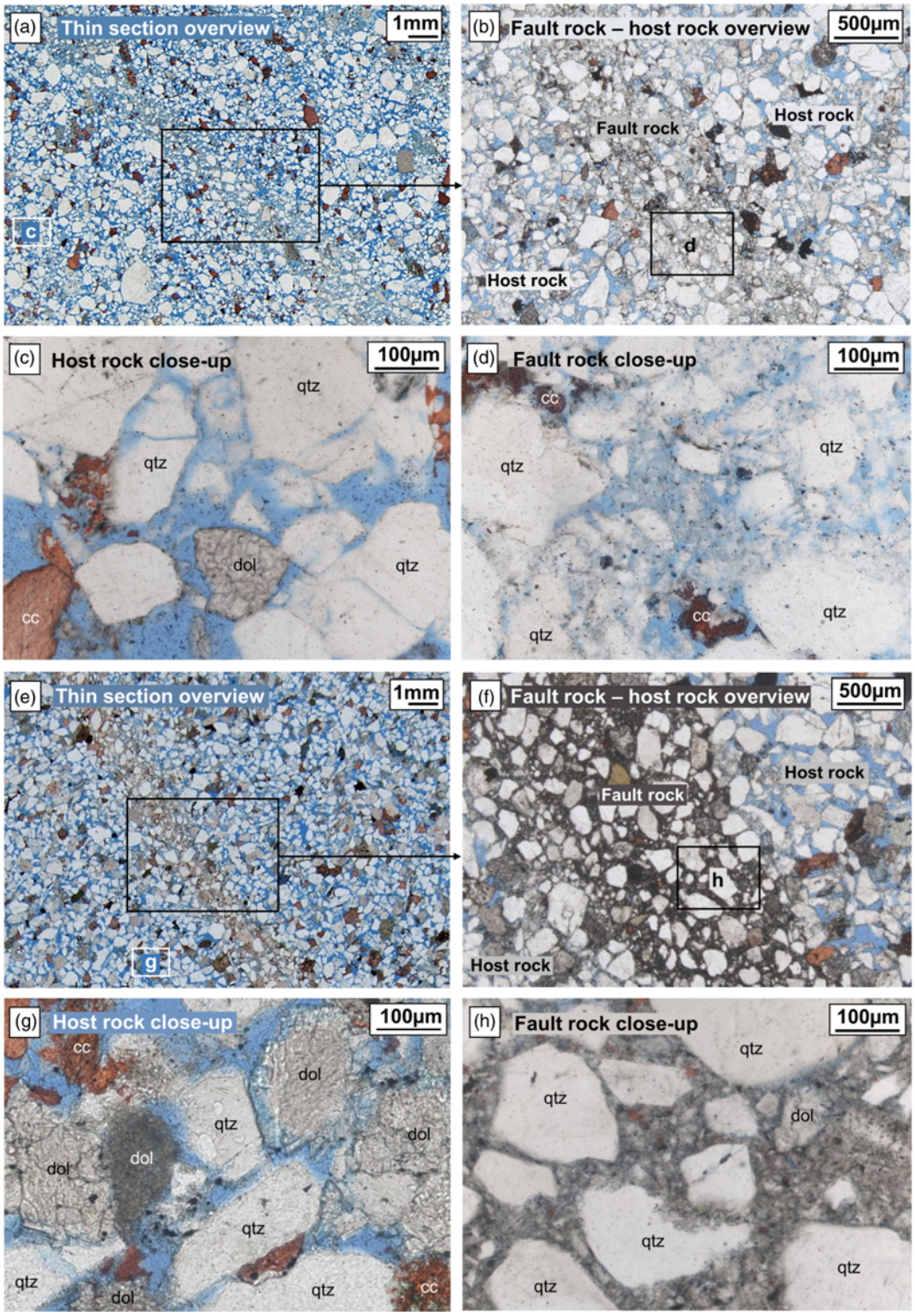

Fig. 7. Photographs from plain-polarized light microscopy: qtz, quartz; dol, dolomite; cc, calcite. Samples with a small permeability reduction are shown in (**a**)–(**d**); samples with a large permeability reduction are displayed in (**e**)–(**h**). Pore space is blue, calcite is stained red. Note the difference in porosity within the fault rocks shown in (d) and (h): while pore space is clearly visible in (d); (h) shows a dense fault rock matrix composed mainly of comminuted quartz, dolomite and ferroan dolomite or ankerite.

(2) fault rock compaction;

(3) cementation by carbonate cements – mainly (ferroan) dolomite.

The processes are discussed in more detail below:

(1) Carbonate grains are generally softer compared to quartz grains due to the different deformation mechanisms of the minerals (Passchier and Trouw 2005). Because of the perfect cleavage of calcite and dolomite compared to the indistinct cleavage of quartz, the more resistant quartz grains could grind down the carbonate grains and act as a natural abrasive within the cataclastic fault zone. Although uniaxial compressive tests on dolomites (e.g. Hatzor *et al.* 1997; Austin and Kennedy 2005; Palchik 2011) and quartz/quartzite (e.g. Singh and Singh 1993; Pierce *et al.* 2009; Kimberley *et al.* 2010) suggest that both lithotypes share similar compressive

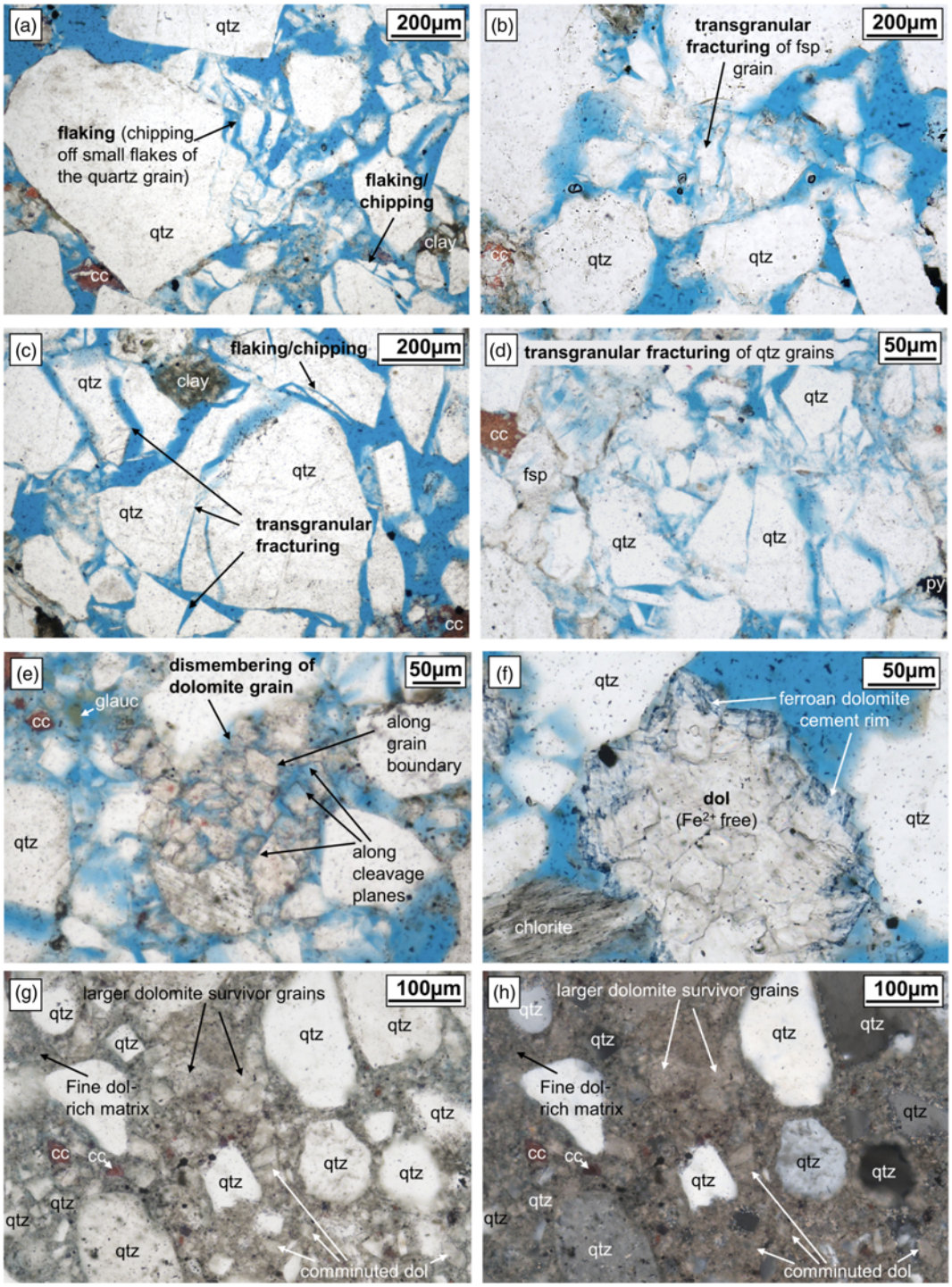

Fig. 8. Photographs from plain- and crossed-polarized light microscopy showing deformation mechanisms and cementation in the studied deformation bands: qtz, quartz; dol, dolomite; cc, calcite; py, pyrite; glauc, glauconite. (**a**)–(**e**) Cataclastic bands with a small permeability reduction. Two main deformation mechanisms were observed: flaking – chipping off parts of the grain (**a**)–(**c**); and transgranular fracturing (**b**)–(**d**). (**e**) Starting dismembering/ comminution of a dolomite grain along existing grain boundaries and cleavage planes. (**f**)–(**h**) Cataclastic bands with a large permeability reduction: (**f**) a dolomite host rock grain that shows a ferroan dolomite cement rim (stained pale blue); fault rock overview in plain-polarized light (**g**) and crossed-polarized light (**h**). Due to the dolomite-rich matrix, comminuted dolomite grains and larger dolomite survivor grains show a low relief and are hard to distinguish from each other in thin section.

strength maxima, several studies have analysed dolomite rock texture and microstructure effects on their mechanical behaviour. Conducting triaxial compression tests on dolomite core samples to study the influence of microstructure on crack initiation stress and ultimate strength, Hatzor *et al.* (1997) showed that the ultimate strength is influenced primarily by porosity and mosaic microstructure of the sample, a term that is used by the authors for the typical dolomite microstructures that can vary from xenotopic over idiotopic to hypidiotopic mosaic microstructure – depending on the single dolomite crystal shapes. Austin and Kennedy (2005) conducted triaxial deformation experiments on texturally diverse dolomites at different confining pressures. Their results show that it is essential to examine grain-boundary microstructures and intragranular flaws prior to making predictions regarding the peak strengths of mineralogical and chemical similar dolomites. Furthermore, studies on deformation

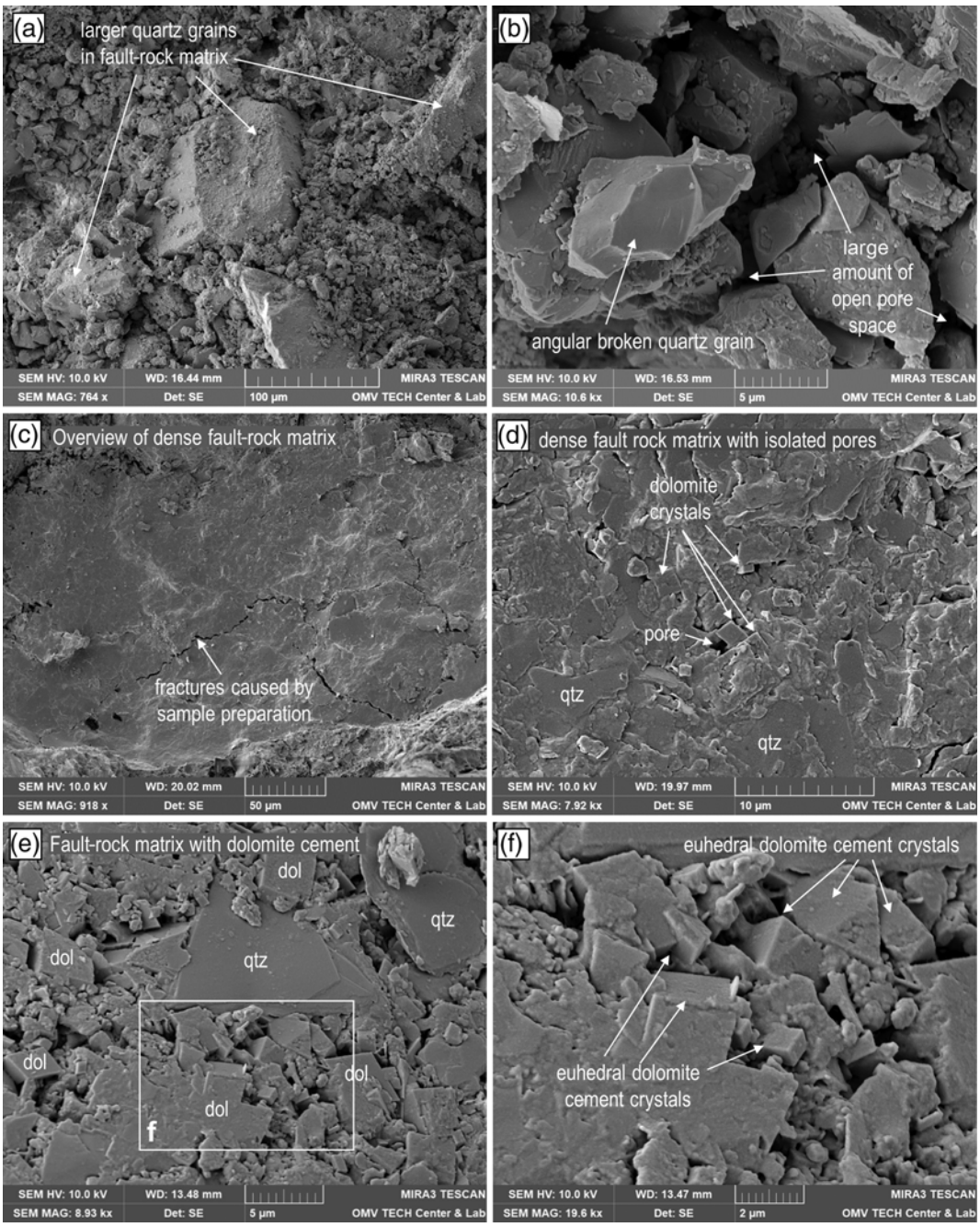

Fig. 9. Scanning electron microscopy (SEM) using secondary electron topography imaging of fault rocks with a small and large permeability reduction. (**a**) & (**b**) Fault rock with a small permeability reduction: (**a**) overview of the fault rock matrix with larger quartz grains; and (**b**) close-up of fault rock matrix grains with quartz grains showing angular broken surfaces; no fault rock cementation was observed in the fault rocks with a small permeability reduction. (**c**)–(**f**) Fault rock with a large permeability reduction: (**c**) overview of the fault rock matrix viewing a semi-planar surface created by a larger broken-out quartz grain; (**d**) dense fault rock matrix composed of small comminuted quartz and dolomite grains, minor amounts of mica, and euhedral dolomite cements. Note that in comparison to (b) only isolated pores are present. (**e**) & (**f**) show close-ups of euhedral dolomite cement crystals, growing between or overgrowing comminuted matrix grains.

processes and fluid-flow behaviour in carbonate fault zones (Schröckenfuchs *et al.* 2015; Bauer *et al.* 2016) have shown that detrital dolomite grains are prone to increased grain-size reduction along pre-existing grain boundaries in the anhedral, xenotopic grain microstructures and along rhombohedral cleavage planes {1011} (Fig. 8e). Since quartz does not exhibit cleavage and most quartz grains in the studied rocks are monocrystalline or lithic quartzite fragments, grains do not have the same internal weakness as observed within the dolomite, which suggests a lower compressive/peak strength for the detrital dolomite grains within the studied samples.

Nevertheless, a moderate amount of larger dolomite survivor grains are visible within the studied fault rocks (Fig. 8g and h). Barber *et al.* (1981) could demonstrate that a dependence on the degree of deformation with regard to the shear angle towards the crystal lattice exists within dolomites, conducting compression tests on single crystals of six different crystallographic orientations under confining pressure. This might explain some of the dolomite survivor grains in the fault rock, together with the fact that most cataclasis fabrics in 'pure lithotypes' (i.e. quartzite or carbonate rock) are typically characterized by larger survivor grains.

Regarding the grain hardness contrast in the studied samples, a similar observation in different lithology is described by Beke *et al.* (2019) investigating deformation band formation in the Pannonian Basin, Hungary: shallowly buried volcanic fragment and feldspar-

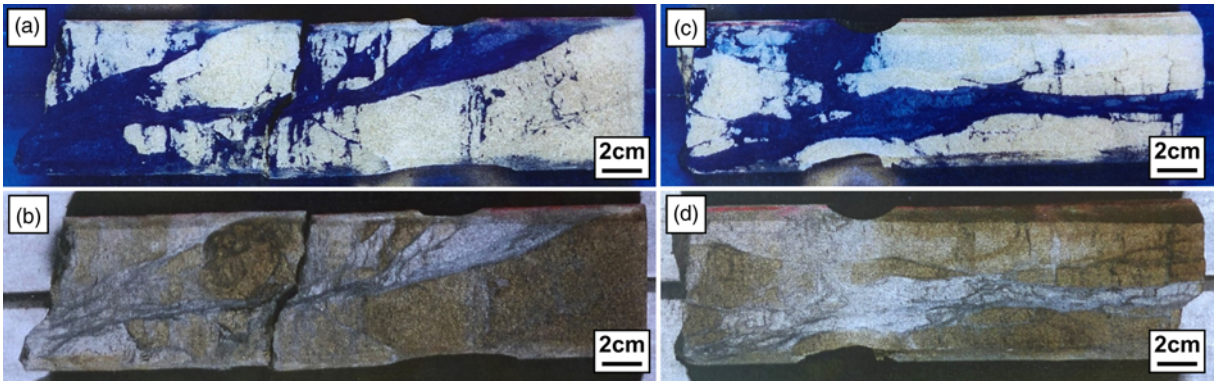

Fig. 10. Photographs of the studied deformation bands under UV light (**a**) &(**c**) and normal light (**b**) & (**d**). The UV light images show clear oil impregnation of the host rock (yellow to white colours), while the deformation band cluster is not impregnated (dark blue colours).

dominated host rocks displayed a greater intensity of cataclasis than quartz-rich siliciclastic rocks. The authors found that grain crushing was more abundant among volcanic fragments, calcite and feldspars due to their good cleavage and fragility, while the more rigid quartz was preferably deformed by abrasion or grain flaking.

(2) Fault rock compaction might act as a second process reducing permeability in the carbonate-rich fault rocks. The deformation bands with a large permeability reduction exhibit a large content of comminuted very-fine-grained dolomite and medium-grained quartz grains (Fig. 8g and h). In comparison to the moderately well-sorted host rock, the deformation bands overall show smaller grain sizes and poorer grain sorting which is favourable for compaction and grain packing (Main *et al.* 2001; Ogilvie and Glover 2001; Tueckmantel *et al.* 2012; Griffiths *et al.* 2016). In the fault rocks with a small permeability reduction, quartz grains and chips do not show grain sizes below 5–10 µm and the grain-supported fabric of larger quartz grains inhibits further compaction (Fig. 7d).

(3) Another process that increases the sealing capacity of the dolomite-rich fault rock samples is the occurrence of dolomite cementation. Micrometre-sized, euhedral and rhomboedric dolomite crystals were observed in the SEM analysis growing in the remaining matrix pore space of the fault rock. It is assumed that the observed cements are growing after the observed grain-size reduction processes within the cataclastic bands, where micrometre-sized host rock dolomite chips could act as nuclei for the onset of cementation.

The fact that cementation only occurs within the fault rock samples which also show a high dolomite content in the host rock but not in the quartz-rich cataclastic fault rocks suggests that the cement is directly sourced from detrital host rock grains. A diagenesis and reservoir quality study on Miocene sandstones in the Vienna Basin conducted by Gier *et al.* (2008) suggested that all mineral cements can be explained by a series of reactions and processes within the host rock that do not require mass flux, fluid flow and movement of material. A similar process was inferred by Weisenberger *et al.* (2019), who showed that carbonate cement in the matrix can be used to accurately predict where fractures are sealed or open using available core or cuttings: out of 44 observed fractures, degradation of 35 fractures (80%) by carbonate cement were predicted correctly based on the cement content of the adjacent matrix. Although our focus in this paper is not on fractures, we suggest a similar correlation between host rock and deformation band fault rock content.

Exner *et al.* (2013) suggested that within deformation bands originating from the central part of the Matzen Field of the Vienna Basin, an external source for cement is likely. Fault rock cements showed a different stable carbon and oxygen isotope signature to the tested carbonate grains in the host rock. The authors proposed fluid migration along faults or mass transfer from underlying or adjoining formations to provide the necessary ions for dolomite cementation. Although we think that an additional external fluid source is possible, it should be considered that the oxygen isotopes would be affected by fractionation during dissolution–reprecipitation and the carbon isotopes could reflect an organic component from within the formation.

We also want to show that although some of the examined samples in this study come from the same field, they differ from the five samples described by Exner *et al.* (2013) in several points: (1) Samples from the Matzen Field in this study originate from the Bockfliess normal fault system, whereas samples from Exner *et al.* (2013) originated from the Matzen Fault Zone. (2) The dolomite content is described as increasing from the host rock (10–20%) to the deformation band (up to 60%) in Exner *et al.* (2013), and therefore the authors classify them as dilation to cementation bands. The dolomite content in the present study is relatively equal in both the host and fault rocks, or lies within the 2% measurement error of the XRD analyses. (3) The rocks studied were classified as cementation bands that had undergone a dilational phase by Exner *et al.* (2013). The current study showed cataclastic grain-size reduction in a more compactional regime with subsequent cementation. The only similarity in the samples from both studies is the overall host rock composition and an increase in ferroan dolomite cement from host rock to fault rock. In our study, XRD results show that the ankerite content rises from the host rock (2.4–6.1 wt%) to the fault rock (7.1–11.6 wt%) which is likely to reflect a similar Fe-rich pore fluid responsible for the fault rock cementation encountered by Gier *et al.* (2008) and Exner *et al.* (2013).

At this stage we assume that the observed contrasts in deformation mechanisms are potentially related to the sampling of different fault systems within the field, although different deformation mechanisms might also occur in dilational and compressional zones along one fault plane.

In the context of fault seal analysis, the studied deformation bands by Exner *et al.* (2013) would theoretically also fit into the subgroup of deformation bands with a high carbonate host rock content and large permeability reduction at shallow depths and low clay content, although the proposed formation mechanisms are different. The described fault rock formation processes nevertheless imply that the mechanisms for permeability reduction within the studied basin, especially in formations with a low clay content at shallow depth, are more complex than anticipated.

Further research is currently ongoing to investigate spatial variations in deformation mechanisms along faults within the Vienna Basin and to progress the understanding of processes such as the observed micro-scale fault rock cementation.

Implication and application for fault seal analysis

Previously conducted fault seal studies in siliciclastic sand–shale formations of the Vienna Basin (OMV internal studies with fault seal software packages) show that for faults with a higher offset, shale smears are likely to be present. No evidence of shale smears could be found in the studied core material. The studied samples might only represent small-scale features with a few millimetres of offset; however, we infer that due to the laboratory results, they should not be neglected for fault seal predictions, especially when dealing with mature oilfields that require artificial lift or enhanced oil recovery (EOR) methods for production. Furthermore, several studies have already highlighted the importance of deformation bands for reservoir fluid flow and confirmed their ability to act as potential structures forming hydrocarbon traps (e.g. Lewis and Couples 1993; Antonellini *et al.* 1999; Fossen and Bale 2007; Torabi *et al.* 2013; Ballas *et al.* 2015; Fossen *et al.* 2017).

Our study shows a clear difference in fault rock permeability between cataclastic deformation bands in dolomite-rich siliciclastic host rocks and host rocks with low to no dolomite content. The encountered quartz-dominated cataclastic bands with a small permeability reduction in the fault rock are unlikely to baffle reservoir fluid flow (20–928 mD) within the studied shallow depths intervals (<2 km). In contrast, the carbonate-rich cataclastic deformation bands will most probably affect reservoir fluid flow (0.3–0.6% mD), especially when clusters of these bands occur (Fig. 10) and if a production time frame is considered.

The difference between the two groups of deformation bands would currently not be predictable by a standard fault seal analysis since all rocks originate from the same rather shallow reservoir level (<2 km), and share the same low V_{shale} content (1.8–4.1 wt%).

If a correlation between carbonate host rock content and fault seal capacity could be confirmed by the ongoing research, a threshold of carbonate content can be defined where fault/deformation band sealing capacities increase significantly. A workflow in addition to a standard fault seal study could allow the sealing capacities in shallow siliciclastic cataclasites to be further constrained by using, for example, calcimetry logs to flag formations exceeding a certain carbonate threshold.

Exner and Tschegg (2012) described deformation bands in poorly consolidated Miocene arkosic sands in the Vienna Basin, where they reported a preferential grain-size reduction of feldspar due to the more efficient fracturing of the weaker sericitized feldspar grains in comparison to quartz. Griffiths *et al.* (2016) reported the preferential cataclasis of K-feldspar grains, which showed lower differential stress than quartz grains, within deformation bands of the Triassic Sherwood Sandstone in the UK. The authors showed that porosity was significantly reduced and pointed out that their study was of direct relevance to the prediction of reservoir quality in several Lower Triassic reservoirs within the East Irish Sea Petroleum Province. Similar observations were reported by Beke *et al.* (2019) for cataclastic deformation bands with volcanic and feldspar grains in siliciclastic host rocks from the Pannonian Basin. All three studies show that an assessment of detrital grain hardness contrast within the host rock might also be extendable to other lithotypes. This could help to distinguish between formations where fluid baffling is likely, and where subseismic faulting and cataclastic deformation bands have less impact on reservoir behaviour – especially at shallow burial depths with low V_{shale} and low fault throw.

The presented study results and discussion also imply that for future fault seal calibration workflows a slightly different approach might be necessary, especially when considering the variations in formation mechanisms described for deformation bands within the Matzen Field (e.g. Exner *et al.* 2013) and the absence of clay smear samples within the screened core material. In order to be able to conduct a meaningful calibration and to improve the interpretation of fault rock distribution on modelled fault planes, geological processes have to be understood for a statistically representative number of samples on the reservoir scale, including rock mechanics and fluid–rock interactions, and need to be upscaled subsequently. Therefore, the sample selection phase is crucial in order to ensure that a reasonable number of samples is analysed and the entire variety of possible fault rocks within a field or basin is captured. We are faced with the additional challenge that representative core material is rare, which is why we are currently widening the focus to also include outcrop analogue-based calibration.

We emphasize that calibration for fault seal analysis should start first at the formation and field scales to avoid early simplification that might lead to a comparison of similar geological features that were caused by different processes at a different geological time.

Conclusions

Conducting a fault seal calibration on core material from the Vienna Basin revealed two dominant fault rock types in the studied deformation bands: cataclasites and phyllosilicate framework fault rocks. Within the cataclastic bands the sealing potential varies strongly, while the shale and mica contents are low (1.8–4.1 wt%). The subgroup of samples with a high carbonate content (21–32 wt %) in the host rock showed a larger permeability reduction in the fault rock than the quartz-dominated subgroup from the same depth interval. A high sealing potential seems to correlate with the detrital dolomite content in the host rock (>10 wt%). Microscopy results suggest that the hardness contrast between the detrital quartz grains and the dolomite grains is responsible for governing the grain-size reduction: cataclasis acts preferably in the dolomites, accompanied by compaction and subsequent cementation. Similar observations for the localization of cataclasis in the weaker grains have been described by other authors (e.g. Exner and Tschegg 2012; Griffiths *et al.* 2016; Beke *et al.* 2019) in deformation bands from siliciclastic host rocks with weaker volcanic fragments or feldspars.

Further investigations to increase the sample number and progress the understanding of cementation processes are still ongoing. Our general aim is to prove if a correlation between carbonate host rock content and fault seal capacity for the studied fields in the Vienna Basin exists. The findings could be used to further constrain fault seal behaviour for shallow (<2 km) siliciclastic formations with a low V_{shale} content that form cataclastic fault rocks. Results might also be extended to other lithotypes with detrital grain hardness contrast in the host rock (stronger quartz v. weaker carbonate rocks, volcanic rocks, feldspars).

Our work has shown that fault seal calibration workflows should be focused first at the formation and field scales to avoid early simplification of observations in complex basins. In addition, the authors want to stress the general importance of data calibration and the constant incorporation of new findings from the reservoir scale for fault seal studies. While existing algorithms and workflows provide us with a great basis to assess and predict fault seal behaviour, our efforts should be focused on thorough data calibration and the assessment of underlying processes that impact the fault seal capacity. This might allow us to find improvements and additional steps of analysis for fields and basins to ensure the ongoing development and improvement of fault seal predictions for the future.

Acknowledgements We acknowledge all technical work conducted in the OMV TECH Center & Laboratory, and especially thank Karl Fabian, Anton Bauer and Andreas Schricker for thin-section preparation and Thomas Gumpenberger and Magdalena Biernat for the porosity and permeability measurements. We would like to thank Russell K. Davies for sparking the idea of conducting a SGR calibration workflow for the Vienna Basin and for providing input for the described workflow. The authors would also like to thank Bernhard Rupprecht for geochemical discussions and support.

Author contributions **TS**: conceptualization (lead), data curation (lead), formal analysis (lead), investigation (lead), methodology (lead), validation (lead), visualization (lead), writing – original draft (lead), writing – review & editing (lead); **VS**: conceptualization (supporting), data curation (supporting), investigation (supporting), methodology (supporting), project administration (lead), supervision (supporting), validation (supporting), writing – review & editing (supporting); **AZ**: conceptualization (supporting), data curation (supporting), investigation (supporting), methodology (supporting), project administration (supporting), supervision (supporting), validation (supporting), writing – review & editing (supporting); **EM**: investigation (supporting), writing – review & editing (supporting); **BG**: writing – review & editing (supporting).

Funding The authors wish to thank OMV Exploration & Production GmbH for the funding of this study within the Research & Development project 'Fault Seal Analysis – Calibration Workflow, 2018'.

Data availability statement All data generated or analysed during this study are included in this published article.

References

Allan, U.S. 1989. Model for hydrocarbon migration and entrapment within faulted structures. *AAPG Bulletin*, **73**, 803–811. https://doi.org/10.1306/44B4A271-170A-11D7-8645000102C1865D.

Antonellini, M.A., Aydin, A. and Orr, L. 1999. Outcrop aided characterization of a faulted hydrocarbon reservoir: Arroyo Grande oil field, California, USA. *American Geophysical Union Geophysical Monograph Series*, **113**, 7–26.

Arzmüller, G., Buchta, S., Ralbovsky, E. and Wessely, G. 2006. The Vienna basin. *AAPG Memoirs*, **84**, 191–204.

Austin, N.J. and Kennedy, L. 2005. Textural controls on the brittle deformation of dolomite: Variations in peak strength. *Geological Society, London, Special Publications*, **243**, 37–49, https://doi.org/10.1144/GSL.SP.2005.243.01.05

Ballas, G., Fossen, H. and Soliva, R. 2015. Factors controlling permeability of cataclastic deformation bands and faults in porous sandstone reservoirs. *Journal of Structural Geology*, **76**, 1–21, https://doi.org/10.1016/j.jsg.2015.03.013

Barber, D.J., Heard, H.C. and Wenk, H.R. 1981. Deformation of dolomite single crystals from 20–800°C. *Physics and Chemistry of Minerals*, **7**, 271–286, https://doi.org/10.1007/BF00311980

Bauer, H., Schröckenfuchs, T.C. and Decker, K. 2016. Hydrogeological properties of fault zones in a karstified carbonate aquifer (Northern Calcareous Alps, Austria). *Hydrogeology Journal*, **24**, 1147–1170, https://doi.org/10.1007/s10040-016-1388-9

Beke, B., Fodor, L., Millar, L. and Petrik, A. 2019. Deformation band formation as a function of progressive burial: Depth calibration and mechanism change in the Pannonian Basin (Hungary). *Marine and Petroleum Geology*, **105**, 1–16, https://doi.org/10.1016/j.marpetgeo.2019.04.006

Bouvier, J.D., Kaars-Sijpesteijn, C.H., Kluesner, D.F., Onyejekwe, C.C. and van der Pal, R.C. 1989. Three-dimensional seismic interpretation and fault sealing investigations, Nun River Field, Nigeria. *AAPG Bulletin*, **73**, 1397–1414, https://doi.org/10.1306/44B4AA5A-170A-11D7-8645000102C1865D.

Bretan, P. 2017. Trap Analysis: an automated approach for deriving column height predictions in fault-bounded traps. *Petroleum Geoscience*, **23**, 56–69, https://doi.org/10.1144/10.44petgeo2016-022

Bretan, P., Yielding, G. and Jones, H. 2003. Using calibrated shale gouge ratio to estimate hydrocarbon column heights. *AAPG Bulletin*, **87**, 397–413, https://doi.org/10.1306/08010201128

Brix, F. and Schultz, O. (eds) 1993. Erdöl und Erdgas in Österreich, 2. Auflage, Verlag Naturhistorisches Museum Wien and F. Berger Horn, Vienna, 688 pp.

Childs, C., Walsh, J.J. *et al.* 2007. Definition of a fault permeability predictor from outcrop studies of a faulted turbidite sequence, Taranaki, New Zealand. *Geological Society, London, Special Publications*, **292**, 235–258, https://doi.org/10.1144/SP292.14

Crawford, B.R., Myers, R.D., Woronow, A., Faulkner, D.R. and Rutter, E.H. 2002. Porosity–permeability relationships in clay-bearing fault gouge. Paper SPE-78214 presented at the SPE/ISRM Rock Mechanics Conference, 20–23 October 2002, Irving, Texas, USA, https://doi.org/10.2118/78214-MS

Decker, K. 1996. Miocene tectonics at the Alpine–Carpathian junction and the evolution of the Vienna Basin. *Mitteilungen der Gesellschaft der Geologie- und Bergbaustudenten der Österreichischen*, **41**, 33–44.

Decker, K., Peresson, H. and Hinsch, R. 2005. Active tectonics and Quaternary basin formation along the Vienna Basin Transform fault. *Quaternary Science Reviews*, **24**, 307–322, https://doi.org/10.1016/j.quascirev.2004.04.012

Dickson, J.A.D. 1965. A modified staining technique for carbonates in thin-section. *Nature*, **205**, 587, https://doi.org/10.1038/205587a0

Eichhubl, P., D'Onfro, P., Aydin, A., Waters, J. and McCarty, D. 2005. Structure, petrophysics, and diagenesis of shale entrained along a normal fault at Black Diamond Mines, California – Implications for fault seal. *AAPG Bulletin*, **89**, 1113–1137, https://doi.org/10.1306/04220504099

Exner, U. and Tschegg, C. 2012. Preferential cataclastic grain size reduction of feldspar in deformation bands in poorly consolidated arkosic sands. *Journal of Structural Geology*, **43**, 63–72, https://doi.org/10.1016/j.jsg.2012.08.005

Exner, U., Kaiser, J. and Gier, S. 2013. Deformation bands evolving from dilation to cementation bands in a hydrocarbon reservoir (Vienna Basin, Austria). *Marine and Petroleum Geology*, **43**, 504–515, https://doi.org/10.1016/j.marpetgeo.2012.10.001

Fisher, Q.J. and Knipe, R.J. 1998. Fault sealing processes in siliciclastic sediments. *Geological Society, London, Special Publications*, **147**, 117–134, https://doi.org/10.1144/GSL.SP.1998.147.01.08

Fossen, H. and Bale, A. 2007. Deformation bands and their influence on fluid flow. *AAPG Bulletin*, **91**, 1685–1700, https://doi.org/10.1306/07300706146

Fossen, H., Soliva, R., Ballas, G., Trzaskos, B., Cavalcante, C. and Schultz, R.A. 2017. A review of deformation bands in reservoir sandstones: geometries, mechanisms and distribution. *Geological Society, London, Special Publications*, **459**, 9–33, https://doi.org/10.1144/SP459.4

Francu, J., Radke, M., Schaefer, R.G., Poelchau, H.S., Caslavsky, J. and Bohacek, Z. 1996. Oil–oil and oil–source rock correlations in the northern Vienna basin and adjacent Carpathian Flysch zone (Czech and Slovak area). *EAGE Special Publications*, **5**, 343–353.

Freeman, B., Yielding, G., Needham, D.T. and Badley, M.E. 1998. Fault seal prediction: the gouge ratio method. *Geological Society, London, Special Publications*, **127**, 19–25, https://doi.org/10.1144/GSL.SP.1998.127.01.03

Fristad, T., Groth, A., Yielding, G. and Freeman, B. 1997. Quantitative fault seal prediction: a case study from Oseberg Syd. *In*: Møller-Pedersen, P. and Koestler, A.G. (eds) *Hydrocarbon Seals: Importance for Exploration and Production*. Norwegian Petroleum Society, Trondheim, Norway, 107–124.

Fuchs, R. and Hamilton, W. 2006. New depositional architecture for an old giant: The Matzen Field, Austria. AAPG Memoirs, **84**, 205–219, https://doi.org/10.1306/985609M843069

Gier, S., Worden, R., Johns, W. and Kurzweil, H. 2008. Diagenesis and reservoir quality of Miocene sandstones in the Vienna Basin, Austria. *Marine and Petroleum Geology*, **25**, 681–695, https://doi.org/10.1016/j.marpetgeo.2008.06.001

Griffiths, J., Faulkner, D.R., Edwards, A.P. and Worden, R.H. 2016. Deformation band development as a function of intrinsic host-rock properties in Triassic Sherwood Sandstone. Geological Society London Special Publications, **435**, 161–176, https://doi.org/10.1144/SP435.11

Harzhauser, M., Grunert, P. *et al.* 2018. Middle and late Badenian palaeoenvironments in the northern Vienna Basin and their potential link to the Badenian Salinity Crisis. *Geologica Carpathica*, **69**, 149–168, https://doi.org/10.1515/geoca-2018-0009

Hatzor, Y.H., Zur, A. and Mimran, Y. 1997. Microstructure effects on microcracking and brittle failure of dolomites. *Tectonophysics*, **281**, 141–161, https://doi.org/10.1016/S0040-1951(97)00073-5

Hinsch, R., Decker, K. and Peresson, H. 2005. 3-D seismic interpretation and structural modeling in the Vienna Basin: implications for Miocene to recent kinematics. *Austrian Journal of Earth Sciences*, **97**, 38–50.

Jiřiček, R. and Seifert, P. 1990. Paleogeography of the Neogene in the Vienna basin and the adjacent part of the foredeep. *In*: Minaříková, D. and Lobitzer, H. (eds) *Thirty Years of Geological Cooperation Between Austria and Czechoslovakia*. Geological Survey, Prague, 89–105.

Kimberley, J., Ramesh, K.T. and Barnouin, O.S. 2010. Visualization of the failure of quartz under quasi-static and dynamic compression. *Journal of Geophysical Research: Solid Earth*, **115**, B08207, https://doi.org/10.1029/2009JB007006

Knipe, R.J. 1992. Faulting processes and fault seal. Norwegian Petroleum Society *(NPF)* Special Publications, **1**, 325–342.

Knipe, R.J. 1997. Juxtaposition and seal diagrams to help analyze fault seals in hydrocarbon reservoirs. *AAPG Bulletin*, **81**, 187–195, https://doi.org/10.1306/522B42DF-1727-11D7-8645000102C1865D.

Ladwein, H.W. 1988. Organic geochemistry of Vienna Basin: Model for hydrocarbon generation in overthrust belts. *AAPG Bulletin*, **72**, 586–599.

Lee, E.Y. and Wagreich, M. 2017. Polyphase tectonic subsidence evolution of the Vienna Basin inferred from quantitative subsidence analysis of the northern and central parts. *International Journal of Earth Sciences (Geologische Rundschau)*, **106**, 687–705, https://doi.org/10.1007/s00531-016-1329-9

Lewis, H. and Couples, G.D. 1993. Production evidence for geological heterogeneities in the Anschutz Ranch East Field, western USA. *Geological Society, London, Special Publications*, **73**, 321–338, https://doi.org/10.1144/GSL.SP.1993.073.01.19

Lindsay, N.G., Walsh, J.J., Watterson, J. and Murphy, F.C. 1993. Outcrop studies of shale smears on fault surfaces. *In*: Flint, S.S. and Bryant, I.D. (eds) *The Geological Modelling of Hydrocarbon Reservoirs and Outcrop Analogues*. Blackwell Scientific, Oxford, UK, 113–123.

Linzer, H.-G., Decker, K., Peresson, H., Dell'Mour, R. and Frisch, W. 2002. Balancing lateral orogenic float of the Eastern Alps. *Tectonophysics*, **354**, 211–237, https://doi.org/10.1016/S0040-1951(02)00337-2

Main, I., Mair, K., Kwon, O., Elphick, S. and Ngwenya, B. 2001. Experimental constraints on the mechanical and hydraulic properties of deformation bands in porous sandstones; a review. *Geological Society, London, Special Publications*, **186**, 43–63, https://doi.org/10.1144/GSL.SP.2001.186.01.04

Manzocchi, T., Walsh, J.J., Nell, P. and Yielding, G. 1999. Fault transmissibility multipliers for flow simulation models. *Petroleum Geoscience*, **5**, 53–63, https://doi.org/10.1144/petgeo.5.1.53

Ogilvie, S.R. and Glover, P.W.J. 2001. The petrophysical properties of deformation bands in relation to their microstructure. *Earth and Planetary*

Science Letters, **193**, 129–142, https://doi.org/10.1016/S0012-821X(01)00492-7

Ogilvie, S.R., Dee, S.J., Wilson, R.W. and Bailey, W.R. 2020. Integrated fault seal analysis: an introduction. *Geological Society, London, Special Publications*, **496**, 1–8, https://doi.org/10.1144/SP496-2020-51

Palchik, V. 2011. On the ratios between elastic modulus and uniaxial compressive strength of heterogeneous carbonate rocks. *Rock Mechanics and Rock Engineering*, **44**, 121–128, https://doi.org/10.1007/s00603-010-0112-7

Passchier, C.W. and Trouw, R.A.J. 2005. *Microtectonics*. 2nd edn. Springer, Berlin, https://doi.org/10.1007/978-3-662-08734-3

Peresson, H. and Decker, K. 1997. Far-field effects of Late Miocene subduction in the Eastern Carpathians: E–W compression and inversion of structures in the Alpine–Carpathian–Pannonian region. *Tectonics*, **16**, 38–56, https://doi.org/10.1029/96TC02730

Pettijohn, F.J., Potter, P.E. and Siever, R. 1973. *Sand and Sandstones*. Springer, New York, http://dx.doi.org/10.1007/978-1-4615-9974-6

Pierce, M., Gaida, M. and DeGagne, D. 2009. Estimation of rock block strength. *In*: Diederichs, M. and Grassell, G. (eds) *RockEng09. Rock Engineering In Difficult Conditions: Proceedings of the 3rd Canada–US Rock Mechanical Symposium, May 2009, Toronto*, Paper 4360.

Poellitzer, S., Florian, T. and Clemens, T. 2009. Revitalising a medium viscous oil field by polymer injection, Pirawarth Field, Austria. Paper SPE-120991 presented at the EUROPEC/EAGE Conference and Exhibition, 8–11 June, Amsterdam, The Netherlands, https://doi.org/10.2118/120991-MS

Ratschbacher, L., Frisch, W., Linzer, H-G and Merle, O. 1991. Lateral extrusion in the eastern Alps, Part 2: Structural analysis. *Tectonics*, **10**, 257–271, https://doi.org/10.1029/90TC02623

Royden, L.H. 1985. The Vienna Basin: a thin-skinned pull-apart basin. *SEPM Special Publications*, **37**, 319–338.

Rupprecht, B.J., Sachsenhofer, R.F., Zach, C., Bechtel, A., Gratzer, R. and Kucher, F. 2019. Oil and gas in the Vienna Basin: hydrocarbon generation and alteration in a classical hydrocarbon province. *Petroleum Geoscience*, **25**, 3–29, https://doi.org/10.1144/petgeo2017-056

Sauer, R., Seifert, P. and Wessely, G. 1992. *Guidebook to Excursions in the Vienna Basin and the Adjacent Alpine–Carpathian Thrustbelt in Austria*. Mitteilugen der Österreichischen Geologischen Gesellschaft, **85**.

Schroeckenfuchs, G. 1975. Hydrogeologie, geochemie und hydrodynamik der formationswässer des raumes Matzen–Schoenkirchen tief. *Erdoel-Erdgas Zeitschrift*, **91**, 299–321.

Schröckenfuchs, T., Bauer, H., Grasemann, B. and Decker, K. 2015. Rock pulverization and localization of a strike-slip fault zone in dolomite rocks (Salzach–Ennstal–Mariazell–Puchberg fault, Austria). *Journal of Structural Geology*, **78**, 67–85, https://doi.org/10.1016/j.jsg.2015.06.009

Schultz, L.G. 1964. *Quantitative Interpretation of Mineralogical Composition from X-ray and Chemical Data for the Pierre Shale*. United States Geological Survey Professional Papers, **391-C**, https://doi.org/10.3133/pp391C

Schumi, W. and Gager, H. 2002. Optimisation of oil production in the mature oil field of Matzen. Paper WPC-32139 presented at the 17th World Petroleum Congress, 1–5 September 2002, Rio de Janeiro, Brazil.

Singh, V.K. and Singh, D.P. 1993. Correlation between point load index and compressive strength for quartzite rocks. *Geotechnical and Geological Engineering*, **11**, 269–272, https://doi.org/10.1007/BF00466369

Soxhlet, F. 1879. Die gewichtsanalytische Bestimmung des Milchfettes. *Dinglers Polytechnisches Journal*, **232**, 461–465.

Sperrevik, S., Gillespie, P.A., Fisher, Q.J., Knipe, R.J. and Halvorsen, T. 2002. Empirical estimation of fault rock properties. *In*: Koestler, A.G. and Hunsdale, R. (eds) *Hydrocarbon Seal Quantification*. *Norwegian Petroleum Society (NPF) Special Publications*, **11**, 109–125.

Strauss, P., Harzhauser, M., Hinsch, R. and Wagreich, M. 2006. Sequence stratigraphy in a classic pull-apart basin (Neogene, Vienna Basin). A 3D seismic based integrated approach. *Geologica Carpathica*, **57**, 185–197.

Torabi, A., Fossen, H. and Braathen, A. 2013. Insight into petrophysical properties of deformed sandstone reservoirs. *AAPG Bulletin*, **97**, 619–637, https://doi.org/10.1306/10031212040

Tueckmantel, C., Fisher, Q.J., Grattoni, C.A. and Aplin, A.C. 2012. Single-and two-phase fluid flow properties of cataclastic fault rocks in porous sandstone. *Marine and Petroleum Geology*, **29**, 129–142, https://doi.org/10.1016/j.marpetgeo.2011.07.009

van Ojik, K., Silvius, A., Kremer, Y. and Shipton, Z.K. 2019. Fault seal behaviour in Permian Rotliegend reservoir sequences: case studies from the Dutch Southern North Sea. *Geological Society, London, Special Publications*, **496**, 9–38, https://doi.org/10.1144/SP496-2018-189

Vrolijk, P.J., Urai, J.L. and Kettermann, M. 2016. Clay smear: Review of mechanisms and applications. *Journal of Structural Geology*, **86**, 95–152, https://doi.org/10.1016/j.jsg.2015.09.006

Weisenberger, T., Eichhubl, P., Laubach, S.E. and Fall, A. 2019. Degradation of fracture porosity in sandstone by carbonate cement, Piceance Basin, Colorado, USA. *Petroleum Geoscience*, **25**, 354–370, https://doi.org/10.1144/petgeo2018-162

Yielding, G. 2002. Shale Gouge Ratio – calibration by geohistory. *Norwegian Petroleum Society (NPF) Special Publications*, **11**, 1–15, https://doi.org/10.1016/S0928-8937(02)80003-0

Yielding, G., Freeman, B. and Needham, D.T. 1997. Quantitative fault seal prediction. *AAPG Bulletin*, **81**, 897–917.

Yielding, G., Bretan, P. and Freeman, B. 2010. Fault seal calibration: a brief review. *Geological Society, London, Special Publications*, **347**, 243–255, https://doi.org/10.1144/SP347.14